Journal of Materials Chemistry C

ROYAL SOCIETY OF CHEMISTRY

PAPER

View Article Online
View Journal | View Issue

Cite this: J. Mater. Chem. C, 2020, 8, 6118

Impact of molecular structure on singlet and triplet exciton diffusion in phenanthroline derivatives†

Deepesh Rai,[a] John S. Bangsund,[a] Javier Garcia Barriocanal[b] and Russell J. Holmes *[a]

Received 11th February 2020,
Accepted 30th March 2020

DOI: 10.1039/d0tc00716a

rsc.li/materials-c

We demonstrate the impact of subtle changes in molecular structure on the singlet and triplet exciton diffusion lengths (L_D) for derivatives of the archetypical electron-transport material 4,7-diphenyl-1,10-phenanthroline (BPhen). Specifically, this work offers a systematic characterization of singlet and triplet exciton transport in identically prepared thin films, highlighting the differing dependence on molecular photophysics and intermolecular spacing. For luminescent singlet excitons, photoluminescence quenching measurements yield an L_D from <1 nm for BPhen, increasing to (5.4 ± 1.2) nm for 2,9-dichloro-4,7-diphenyl-1,10-phenanthroline (BPhen-Cl_2) and (3.9 ± 1.1) nm for 2,9-dimethyl-4,7-diphenyl-1,10-phenanthroline (BCP). The diffusion of dark triplet excitons is probed using a phosphorescent sensitizer-based method where triplets are selectively injected into the material of interest, with those migrating through the material detected *via* energy transfer to an adjacent, phosphorescent sensitizer. Interestingly, the triplet exciton L_D decreases from (15.4 ± 0.4) nm for BPhen to (8.0 ± 0.7) nm for BPhen-Cl_2 and (4.0 ± 0.5) nm for BCP. The stark difference in behavior observed for singlets and triplets with functionalization is explicitly understood using long-range Förster and short-range Dexter energy transfer mechanisms, respectively.

1. Introduction

Excitons play a central role in the design of optoelectronic devices based on organic semiconductors, with exciton spin strongly determining the luminescence and transport characteristics of the component active materials.[1–5] In terms of exciton transport, spin singlet and triplet excitons diffuse *via* different mechanisms, due mainly to the fact that singlets may undergo radiative recombination while triplets are often dark.[6] This difference in mechanism also implies that the handles available for tuning the exciton diffusion length (L_D) may enhance the transport of one spin state while not favorably impacting the other.[7] Reduced intermolecular spacing is typically considered as a route to improve exciton transport however, even here care must be taken to avoid increasing non-radiative decay and reducing the exciton lifetime. Several studies have reported on the role of molecular functionalization and crystallization in enhancing singlet exciton transport.[8–16] There are however fewer studies of triplet excitons as they are often non-radiative and hence incompatible with common photoluminescence-based techniques. Furthermore, few efforts have sought to systematically compare the role of molecular functionalization on the diffusion of singlet and triplet states.[17,18] As such, there exists a need for experimental methodologies that permit the investigation of singlet and triplet diffusion in a common set of samples that could experimentally elucidate fundamental differences in transport behavior between these states.

Exciton diffusion is frequently described as an ensemble of intermolecular energy transfer events with the diffusivity (D) written in terms of the energy transfer rate (k_{ET}) as:[6,10,19]

$$D = \frac{1}{6}\sum_{N} d^2 k_{ET}(d) = \frac{{L_D}^2}{\tau} \quad (1)$$

where d is the intermolecular spacing assuming a cubic lattice, τ is the exciton lifetime, and N is the number of molecular hopping sites. For fluorescent singlet excitons, energy transfer *via* dipole coupling (Förster transfer) often dominates, with an energy transfer rate given as:[6,20]

$$k_F(d) = \frac{1}{\tau}\left(\frac{R_0}{d}\right)^6 \quad (2)$$

where τ is the exciton lifetime and R_0 is the Förster radius which is separately defined as:[6,12]

$${R_0}^6 = \frac{9\eta_{PL}\kappa^2}{128\pi^5}\int\frac{\lambda^4 F_D(\lambda)\sigma_A(\lambda)d\lambda}{n(\lambda)^4} \quad (3)$$

[a] Department of Chemical Engineering and Materials Science, University of Minnesota, Minneapolis, MN 55455, USA. E-mail: rholmes@umn.edu
[b] Characterization Facility, University of Minnesota, Minneapolis, MN 55455, USA

† Electronic supplementary information (ESI) available: Simulated and experimental X-ray reflectivity (XRR) data used to obtain thin film density. Simulated outcoupled photoluminescence efficiency ratio as a function of active layer thickness for calculation of transport efficiency. Triplet exciton lifetimes extracted from transient photoluminescence. Thin film surface morphology extracted using AFM. See DOI: 10.1039/d0tc00716a

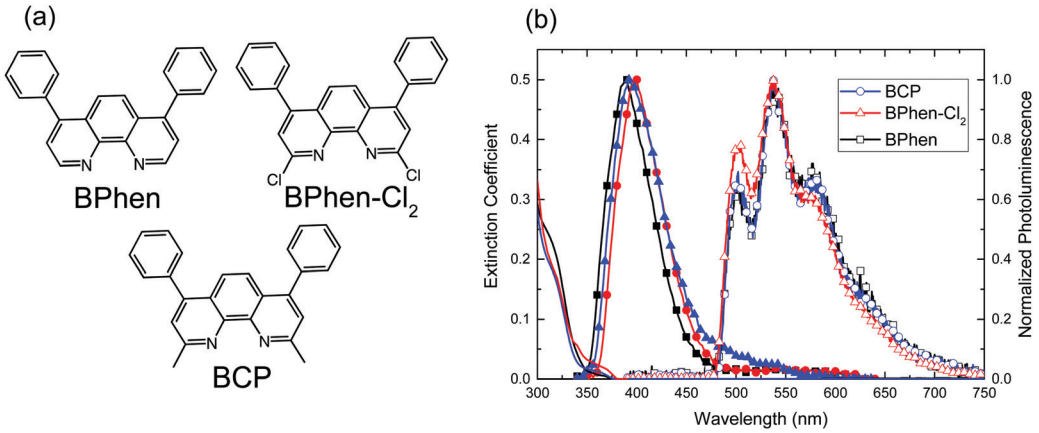

Fig. 1 (a) Molecular structures of the phenanthroline derivatives considered in this work. (b) Thin film fluorescence (closed symbols) and extinction spectra (solid lines) for the molecules in (a) taken at room temperature. Low temperature phosphorescence spectra (open symbols) are collected at 10 K at long-times after pulsed excitation to avoid detection of fluorescence.

where η_{PL} is the photoluminescence efficiency, κ is the dipole orientation factor (taken as $0.845\sqrt{\frac{2}{3}}$ for randomly oriented rigid dipoles),[21] n is the wavelength dependent refractive index of the donor film, F_D is the normalized fluorescence spectrum, σ_A is the acceptor absorption cross-section, and λ is the wavelength. It is clear in eqn (2) and (3) that a change in intermolecular spacing can have a nuanced effect on Förster transfer. For example, prior work has shown that an increase in L_D can be observed with increased spacing due to favorable increases in the exciton lifetime and self-Förster radius with spacing.[12,22,23]

In materials with non-luminescent triplet excitons, energy transfer is typically mediated by electron exchange interactions in the form of Dexter transfer. The subsequent transfer rate is defined as:[6,19,24]

$$k_D = \frac{2\pi}{\hbar}K^2 \exp\left(-\frac{2d}{L}\right)\int F_D(E)\sigma_A(E)\mathrm{d}E \qquad (4)$$

where F_D and σ_A are normalized donor and acceptor emission and absorption spectra, respectively, d is the intermolecular separation, L is the effective average orbital radius for the excited and unexcited state of donor and acceptor, and K is a constant that reflects the specific orbital interactions. Clearly, increased intermolecular spacing hinders the triplet hopping rate *via* electron exchange, making possible different trends in the dependence of L_D on d for singlets and triplets.

In this work, we examine singlet and triplet exciton diffusion as a function of molecular functionalization in phenanthroline derivatives, offering a useful contrast of the factors governing the migration of each state. Phenanthrolines have long been used as electron transport materials and exciton blocking layers in organic light-emitting devices (OLEDs) and organic photovoltaic cells (OPVs), and are examined here for the availability of several derivatives namely, 4,7-diphenyl-1,10-phenanthroline (BPhen), 2,9-dichloro-4,7-diphenyl-1,10-phenanthroline (BPhen-Cl_2), and 2,9-dimethyl-4,7-diphenyl-1,10-phenanthroline (BCP), where steric bulk and intermolecular spacing are tailored by substitution of –H, –Cl and –CH_3 on the phenanthroline core (Fig. 1a). Changes in intermolecular spacing also lead to changes in molecular photophysics, and measurements of exciton transport are complemented by detailed spectroscopic investigations. Thus, a systematic understanding for the role of functionalization on singlet and triplet diffusion is established.

2. Experimental section

BPhen, BPhen-Cl_2, BCP, 1,3-bis(*N*-carbazolyl)benzene (mCP), [(4,6-difluorophenyl)pyridinato-C2,N](picolinato)iridium(III) (FIrpic), and 1,4,5,8,9,11-hexaazatriphenylene hexacarbonitrile (HATCN) are purchased from Luminescence Technology Corporation; platinum octaethylporphyrin (PtOEP) is purchased from Frontier Scientific. For thickness dependent PL quenching measurements, a unity quenching efficiency is assumed for HATCN due to favorable energy offset for electron transfer.[23,25] Photoluminescence spectra are measured in a Photon Technology International QuantaMaster 400 Fluorometer equipped with a photomultiplier detection system. Structures are excited using a Xe lamp attached to a monochromator, at an angle of 70° from substrate normal. Photoluminescence efficiencies are measured in an integrating sphere using a previously published methodology.[26] The thin film thicknesses and material optical constants are measured using a J. A. Woollam variable-angle spectroscopic ellipsometer. Singlet exciton lifetimes are measured using a PicoQuant time correlated single photon counting (TCSPC) system, pumped using a regeneratively amplified Ti:sapphire laser system producing ~80 fs, λ = 900 nm pulses at a repetition rate of 40 MHz. A λ = 300 nm excitation pulse is then obtained using a nonlinear harmonic generation system equipped with a BBO crystal for tripling the frequency of the excited pulse. A closed cycle Janis CSS-150 He optical cryostat is used to measure triplet photoluminescence spectra and lifetimes at 10 K. Samples are pumped at a wavelength of λ = 337 nm using a N_2 laser which provides

~1 ns pulse width. The emission spectrum from the sample is detected using a FERGIE integrated spectrograph (Princeton Instruments), with spectrum acquisition triggered externally with a pulse generator after a 5 ms delay from the laser pulse. The repetition rate of the laser is kept at 0.25 Hz. Triplet photoluminescence spectra are measured for different delay times to obtain the triplet lifetime. X-ray reflectivity is measured on a 20 nm-thick film of the active material deposited on a Si substrate using a PANalytical X'pert Pro instrument. The experimental data is simulated using GenX software to obtain thin film density, surface roughness and film thickness. The film thickness is independently checked with values from ellipsometry. The film crystallinity is checked using X-ray diffraction measurements at an incident angle of 8 degrees, while the sample is scanned using a 2D detector which spans from 2θ = 1 degree to 53 degrees. Experimental data for singlet and triplet L_D measurements is fit using a non-linear least square methodology where error in the fit value represents a 95% confidence interval.

3. Results and discussion

Fig. 1b shows the thin film extinction coefficient and photoluminescence (PL) behavior of the active materials of interest in this work. The PL collected at room temperature is fluorescence from the singlet state. The phosphorescence spectra shown in Fig. 1b were collected at 10 K at long times under pulsed laser excitation. Spectrum acquisition was triggered by a pulse generator with a 5 ms delay after the laser pulse to reject short time luminescence and only collect long-lived triplet phosphorescence. As-deposited films showed no evidence of crystallinity in X-ray diffraction (XRD) measurements. Fine differences in the intermolecular spacing with functionalization were probed by measuring film density using X-ray reflectivity (XRR). The film thickness, density, and roughness are used as fitting parameters for XRR experimental data analysis. The fit parameters along with independent measurements of film thickness using ellipsometry are shown in Table S1 (ESI†). XRR analysis yields extracted molecular densities of (1.87 ± 0.03) nm^{-3} for BCP, (2.04 ± 0.03) nm^{-3} for BPhen-Cl_2, and (2.26 ± 0.03) nm^{-3} for BPhen, consistent with previous reports for BPhen and BCP.[27]

The singlet L_D for each material of interest is extracted using thickness dependent PL quenching.[28,29] Thin film fluorescence is measured with and without the presence of an adjacent top quenching layer of HATCN.[28] The PL ratio (quenched to unquenched) is measured as a function of active layer thickness and fit to yield the singlet L_D. Table 1 lists the singlet L_D values extracted for BPhen and its derivatives, obtained by analytical modelling of the associated PL ratio (Fig. 2). Extracted values of L_D are < 1 nm for BPhen, (3.9 ± 1.1) nm for BCP, (5.4 ± 1.2) nm for BPhen-Cl_2. It is worth noting that if fit explicitly, the data in Fig. 2 for BPhen yields $L_D = (0.8 \pm 0.3)$ nm. This value is below the estimated resolution limit of 1 nm of the technique.

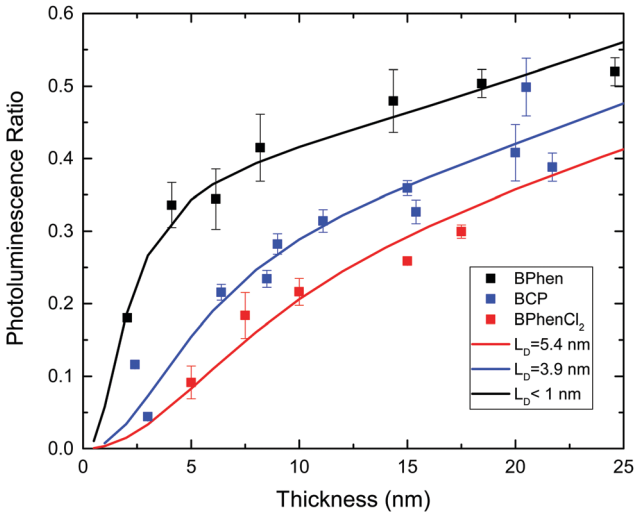

Fig. 2 Photoluminescence ratios (with and without an adjacent HATCN quenching layer) for BPhen and its derivatives with the corresponding exciton diffusion length (L_D) extracted from the data.

The observed trend in singlet L_D can be considered in terms of Förster theory by considering how changes in intermolecular spacing and the self-R_0 (Table 1) impact L_D. Singlet L_D values for the BPhen derivatives scale linearly with the ratio R_0^3/d^2 as expected based on eqn (1) and (2). This ratio is largest for BPhen-Cl_2, which reflects a high degree of spectral overlap between fluorescence and absorption spectra.

Fig. 3a shows the device architecture for measuring the triplet L_D in BPhen and its derivatives using a phosphorescent sensitizer based method.[30,31] A layer of FIrpic (triplet energy, E_T = 2.65 eV) injects triplets into the phenanthroline of interest (E_T = 2.47 eV for all three materials). Injected triplets that migrate through the full thickness of the active layer are detected using a sensitizer of PtOEP (E_T = 1.9 eV)[32] doped in the wide energy gap host mCP (E_T = 2.9 eV). Exciton diffusion in the active layer is defined in terms of a transport efficiency (η_T) as:[31,32]

$$\eta_T = \frac{\Delta PL^{PtOEP}}{\Delta PL^{FIrpic}} \times \frac{\eta^{PL}_{Firpic}}{\eta^{PL}_{PtOEP}} \quad (5)$$

where η^{PL}_{Firpic} and η^{PL}_{PtOEP} are the outcoupled PL efficiencies of the FIrpic and PtOEP layers. The outcoupling efficiency ratio in the absence of the active layer is experimentally determined by directly injecting excitons from FIrpic to PtOEP using a previously published method.[30,31] The variation in outcoupling efficiency as a function of

Table 1 Exciton transport and photophysical parameters for phenanthroline thin films

Materials	Singlet L_D (nm)	Singlet τ (ns)	Singlet η_{PL} (%)	Self-R_0 (nm)	Triplet L_D (nm)	Triplet τ (ms) (10 K)
BPhen	<1	0.58 ± 0.03	2.5 ± 0.5	0.59 ± 0.01	15.4 ± 0.4	455.2 ± 7.9
BPhen-Cl_2	5.4 ± 1.2	0.48 ± 0.01	9.4 ± 0.9	0.84 ± 0.01	8.0 ± 0.7	313.7 ± 19.5
BCP	3.9 ± 1.1	1.24 ± 0.01	21.6 ± 2.2	0.85 ± 0.01	4.0 ± 0.5	633.1 ± 59.8

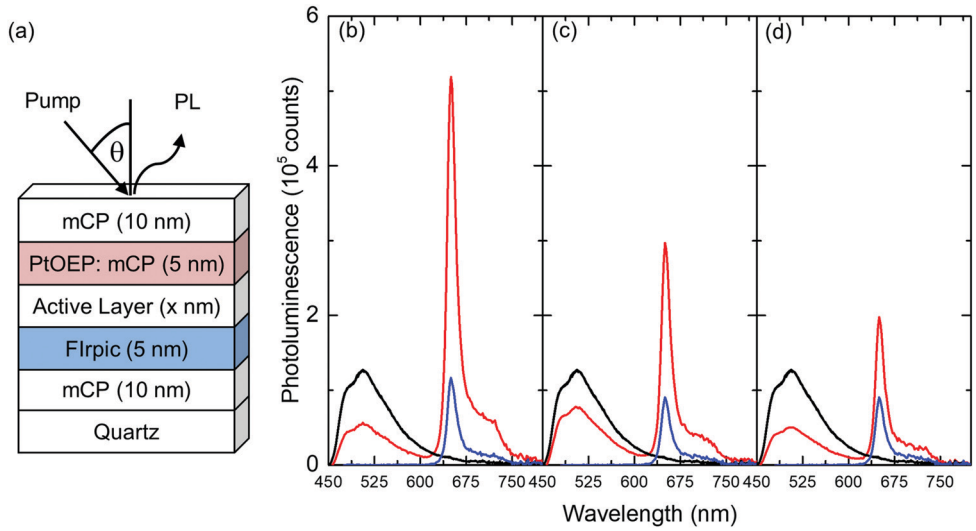

Fig. 3 (a) Multilayer thin film architecture for investigating the triplet L_D for BPhen and its derivatives. The structure is pumped at a wavelength of λ = 430 nm where a majority of excitons are generated in the FIrpic injection layer. The excitons that diffuse through BPhen and its derivatives are detected using 5 wt% PtOEP doped in mCP. The photoluminescence spectra are collected for the multilayer structures FIrpic/mCP (10 nm)/mCP (black line); FIrpic/active layer (10 nm)/5 wt% PtOEP:mCP (red line) and mCP/active layer (10 nm)/5 wt% PtOEP:mCP (blue line), where the active layer is (b) BPhen, (c) BPhen-Cl_2 or (d) BCP.

active layer thickness is calculated using Setfos 4.6 (Fluxim) software (Fig. S2, ESI†).

Fig. 3b shows PL spectra for FIrpic and PtOEP with an active layer of BPhen, BPhen-Cl_2, or BCP, for cases with and without injection of excitons into the active layer. The increase in PL from PtOEP due to energy transfer from FIrpic can be isolated from direct optical excitation (*i.e.* where the injection layer of FIrpic is replaced with mCP). Kinetic Monte Carlo (KMC)[30,31] modelling of the experimentally measured η_T as a function of active layer thickness results in triplet L_D values of (15.4 ± 0.4) nm for BPhen, (8.0 ± 0.7) nm for BPhen-Cl_2, and (4.0 ± 0.5) nm for BCP (Fig. 4a).

The mechanism for energy transfer can be understood by first decoupling the exciton lifetime and the diffusivity. The triplet lifetime for each material is shown in Table 1 and was determined from low temperature transient phosphorescence. The trend in triplet lifetime (Table 1 and Fig. S3, ESI†) cannot alone explain the observed variation in triplet L_D, suggesting a change in diffusivity. This could come from changes in optical overlap, the molecular orbital radius, and the intermolecular spacing. Changes in film roughness could also lead to differences in the extracted L_D, but this possibility is ruled out using atomic force microscopy (AFM) of as-deposited films of each active material. Films of all materials studied here show a featureless morphology with root mean square roughness < 1 nm (Fig. S4, ESI†).

The variation in triplet diffusivity is considered in terms of differences in intermolecular spacing. Indeed, eqn (1) and (4) suggest an exponential relationship between triplet diffusivity and intermolecular spacing, and hence the linearity of a semi-log plot between triplet (L_D/d) and intermolecular spacing can be used to check the validity of the assumed diffusion model. Fig. 4b shows a linear fit between a semi-log plot of L_D/d and intermolecular spacing. The value of d is determined by taking the cube root of the molecular density $\left(\sqrt[3]{\frac{1}{\rho}}\right)$ as measured using XRR. The intermolecular spacing varies in increasing order as (7.62 ± 0.04) Å for BPhen, (7.88 ± 0.04) Å for BPhen-Cl_2 and (8.11 ± 0.04) Å for BCP, corresponding-well with the concomitant reduction in triplet L_D. The observed linear trend also holds for a mixture of 10 wt% BCP in BPhen, suggesting that BCP and BPhen form a substitutional solid solution. The slope yields the molecular orbital radius as (0.37 ± 0.04 Å) (Fig. 4b). This value is consistent with previous reports for Dexter transfer yielding ~0.39 Å to 2.1 Å.[33–37]

4. Conclusions

We present a study connecting the measured singlet and triplet exciton diffusion length with changes in molecular structure and intermolecular spacing. Singlet L_D values are extracted using thickness dependent photoluminescence quenching measurements while triplet L_D values are extracted using a phosphorescent sensitizer-based methodology. For the phenanthroline derivatives considered here, the intermolecular spacing varies in increasing order as (7.62 ± 0.04) Å for BPhen, (7.88 ± 0.04) Å for BPhen-Cl_2, and (8.11 ± 0.04) Å for BCP. The singlet L_D increases from L_D < 1 nm for BPhen to (5.4 ± 1.2) nm for BPhen-Cl_2, and (3.9 ± 1.1) nm BCP, while the triplet L_D decreases from (15.4 ± 0.4) nm for BPhen to (8.0 ± 0.7) nm for BPhen-Cl_2, and (4.0 ± 0.5) nm for BCP. The variation in singlet L_D is understood using Förster transfer, considering changes in the intermolecular spacing as well as factors including the photoluminescence efficiency and optical overlap. The decrease in triplet L_D is understood more simply using Dexter transfer

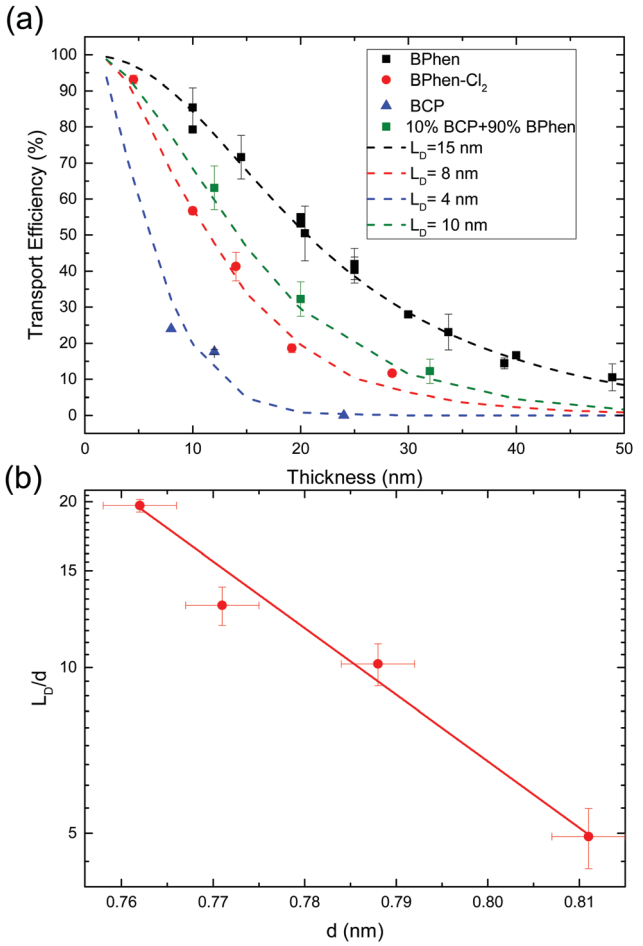

Fig. 4 (a) Experimental (symbols) and simulated (lines) transport efficiency as a function of active layer thickness for different values of the triplet L_D. (b) Measured triplet L_D divided by the intermolecular spacing (d) plotted as a function of d for BPhen and its derivatives. The solid line is a linear fit through the data points.

where the rate of energy transfer scales exponentially with intermolecular spacing. This work offers insight into the significant and differing role changes in molecular structure can play for singlet and triplet exciton transport.

Conflicts of interest

There are no conflicts of interest to declare.

Acknowledgements

This work was supported by National Science Foundation (NSF) Solid-State and Materials Chemistry under DMR-1708177 and Electronics, Photonics and Magnetic Devices under ECCS-1509121. J. S. B. acknowledges support from the NSF Graduate Research Fellowship under Grant No 00039202. R. J. H. would like to acknowledge support from a Leverhulme Trust Visiting Professorship at the University of Cambridge and a Visiting Fellowship at Clare Hall, University of Cambridge. The authors acknowledge C. P. Clark for X-ray diffraction measurements and Dr A. Healy for measuring singlet exciton lifetimes using TCSPC.

References

1 H. Uoyama, K. Goushi, K. Shizu, H. Nomura and C. Adachi, *Nature*, 2012, **492**, 234–238.
2 F. B. Dias, K. N. Bourdakos, V. Jankus, K. C. Moss, K. T. Kamtekar, V. Bhalla, J. Santos, M. R. Bryce and A. P. Monkman, *Adv. Mater.*, 2013, **25**, 3707–3714.
3 D. Di, A. S. Romanov, L. Yang, J. M. Richter, J. P. H. Rivett, S. Jones, T. H. Thomas, M. Abdi Jalebi, R. H. Friend, M. Linnolahti, M. Bochmann and D. Credgington, *Science*, 2017, **356**, 159–163.
4 C. Adachi, M. A. Baldo, M. E. Thompson and S. R. Forrest, *J. Appl. Phys.*, 2001, **90**, 5048–5051.
5 A. Rao, M. W. B. Wilson, J. M. Hodgkiss, S. Albert-Seifried, H. Bässler and R. H. Friend, *J. Am. Chem. Soc.*, 2010, **132**, 12698–12703.
6 S. M. Menke and R. J. Holmes, *Energy Environ. Sci.*, 2014, **7**, 499–512.
7 S. R. Yost, E. Hontz, S. Yeganeh and T. Van Voorhis, *J. Phys. Chem. C*, 2012, **116**, 17369–17377.
8 S.-B. Rim, R. F. Fink, J. C. Schöneboom, P. Erk and P. Peumans, *Appl. Phys. Lett.*, 2007, **91**, 173504.
9 R. R. Lunt, J. B. Benziger and S. R. Forrest, *Adv. Mater.*, 2010, **22**, 1233–1236.
10 H. Najafov, B. Lee, Q. Zhou, L. C. Feldman and V. Podzorov, *Nat. Mater.*, 2010, **9**, 938.
11 P. M. Beaujuge and J. M. J. Fréchet, *J. Am. Chem. Soc.*, 2011, **133**, 20009–20029.
12 T. K. Mullenbach, K. A. McGarry, W. A. Luhman, C. J. Douglas and R. J. Holmes, *Adv. Mater.*, 2013, **25**, 3689–3693.
13 O. V. Mikhnenko, J. Lin, Y. Shu, J. E. Anthony, P. W. M. Blom, T.-Q. Nguyen and M. A. Loi, *Phys. Chem. Chem. Phys.*, 2012, **14**, 14196.
14 M. Grover and R. Silbey, *J. Chem. Phys.*, 1971, **54**, 4843–4851.
15 Y. Long, G. J. Hedley, A. Ruseckas, M. Chowdhury, T. Roland, L. A. Serrano, G. Cooke and I. D. W. Samuel, *ACS Appl. Mater. Interfaces*, 2017, **9**, 14945–14952.
16 Z. Masri, A. Ruseckas, E. V. Emelianova, L. Wang, A. K. Bansal, A. Matheson, H. T. Lemke, M. M. Nielsen, H. Nguyen, O. Coulembier, P. Dubois, D. Beljonne and I. D. W. Samuel, *Adv. Energy Mater.*, 2013, **3**, 1445–1453.
17 P. Irkhin and I. Biaggio, *Phys. Rev. Lett.*, 2011, **107**, 017402.
18 C. Wu, P. I. Djurovich and M. E. Thompson, *Adv. Funct. Mater.*, 2009, **19**, 3157–3164.
19 R. C. Powell and Z. G. Soos, *J. Lumin.*, 1975, **11**, 1–45.
20 T. Förster, *Discuss. Faraday Soc.*, 1959, **27**, 7–17.
21 J. Baumann and M. D. Fayer, *J. Chem. Phys.*, 1986, **85**, 4087–4107.
22 S. M. Menke, W. A. Luhman and R. J. Holmes, *Nat. Mater.*, 2013, **12**, 152–157.
23 S. M. Menke and R. J. Holmes, *ACS Appl. Mater. Interfaces*, 2015, **7**, 2912–2918.

24 D. L. Dexter, *J. Chem. Phys.*, 1953, **21**, 836.
25 T. Zhang, D. B. Dement, V. E. Ferry and R. J. Holmes, *Nat. Commun.*, 2019, **10**, 1156.
26 Y. Kawamura, H. Sasabe and C. Adachi, *Jpn. J. Appl. Phys.*, 2004, **43**, 7729–7730.
27 H. F. Xiang, Z. X. Xu, V. A. L. Roy, C. M. Che and P. T. Lai, *Rev. Sci. Instrum.*, 2007, **78**, 034104.
28 P. Peumans, A. Yakimov and S. R. Forrest, *J. Appl. Phys.*, 2003, **93**, 3693–3723.
29 R. R. Lunt, N. C. Giebink, A. A. Belak, J. B. Benziger and S. R. Forrest, *J. Appl. Phys.*, 2009, **105**, 053711.
30 D. Rai and R. J. Holmes, *Phys. Rev. Appl.*, 2019, **11**, 014048.
31 D. Rai and R. J. Holmes, *J. Mater. Chem. C*, 2019, **7**, 5695–5701.
32 R. J. Holmes, S. R. Forrest, Y.-J. Tung, R. C. Kwong, J. J. Brown, S. Garon and M. E. Thompson, *Appl. Phys. Lett.*, 2003, **82**, 2422–2424.
33 P. B. Merkel and J. P. Dinnocenzo, *J. Phys. Chem. A*, 2008, **112**, 10790–10800.
34 Z. Li, W. E. Lee and W. C. Galley, *Biophys. J.*, 1989, **56**, 361–367.
35 G. B. Strambini and W. C. Galley, *Chem. Phys. Lett.*, 1976, **39**, 257–260.
36 C. Curutchet and A. A. Voityuk, *J. Phys. Chem. C*, 2012, **116**, 22179–22185.
37 A. R. S. Kandada, G. Grancini, A. Petrozza, S. Perissinotto, D. Fazzi, S. S. K. Raavi and G. Lanzani, *Sci. Rep.*, 2013, **3**, 2073.